Materials Advances

PAPER

View Article Online
View Journal | View Issue

Cite this: *Mater. Adv.*, 2025, **6**, 6416

Enhanced catalytic performance of MnO_2 nanowires for soot combustion by cobalt incorporation

Issara Sereewatthanawut,[ab] Chalempol Khajonvittayakul,[c] Notsawan Swadchaipong,[c] Vut Tongnan,[c] Panupun Maneesard,[c] Rossarin Ampairojanawong,[c] Ammarika Makdee,[c] Tawiwan Kangsadan,[c] Matthew Hartley[d] and Unalome Wetwatana Hartley*[c]

The impact of cobalt (Co) doping on the structure, redox, and catalytic properties of MnO_2 nanowires (NWs) for soot combustion was investigated. XRD analysis revealed that pure MnO_2 NWs exhibit a mixture of major α-MnO_2 and minor γ-MnO_2 phases, while Co doping at 10 mol% enhanced the γ-MnO_2 content and induced unbalanced charge in the MnO_2 structure *via* Mn substitution by Co, which induced lattice defects, including oxygen vacancies. SEM images confirmed the successful formation of nanowire morphology using the hydrothermal method for all prepared catalysts. H_2-TPR profiles demonstrated enhanced reducibility and oxygen mobility in Co-doped catalysts, attributed to synergistic effects between Mn and Co species and increased oxygen vacancy concentration. The soot oxidation mechanism suggested that oxygen vacancies and mobility play a key role in sustaining lattice oxygen activation. Catalytic activity tests for soot combustion revealed that 10 mol% Co-doped MnO_2 NWs achieved the lowest T_{50} (363 °C), outperforming both pure MnO_2 NWs and 20 mol% Co-doped MnO_2 NWs, due to optimized structural, porosity, and redox properties, and oxygen mobility. Post-reaction investigations demonstrated that the nanowire catalyst might provide sustained catalytic performance over several reaction cycles by converting to catalytically active Mn_3O_4 without morphological degradation.

Received 13th May 2025,
Accepted 3rd August 2025

DOI: 10.1039/d5ma00480b

rsc.li/materials-advances

1. Introduction

Particulate matter (PM), commonly referred to as soot, is a major pollutant found in diesel engine exhaust emissions. It comprises a complex mixture of constituents, primarily elemental carbon, along with volatile organic compounds, sulfates, and trace metallic ashes.[1–3] The inhalation of PM has been associated with a wide range of adverse health effects, including respiratory ailments, cardiovascular disease, exacerbation of asthma, and even carcinogenesis.[4–6] Due to these serious health concerns, stringent environmental regulations have been established to limit soot emissions from diesel-powered vehicles. For instance, since 2009, the European Union has enforced a maximum allowable particulate emission level of 0.005 g km^{-1} for both passenger cars and light-duty commercial vehicles equipped with diesel engines.[7] Consequently, the development of efficient and practical technologies for the abatement of soot emissions has become a critical area of environmental research.

To meet these increasingly strict emissions standards, diesel particulate filters (DPFs) have been widely adopted as an integral component of diesel vehicle exhaust after-treatment systems. DPFs are typically ceramic filters designed with a honeycomb-like monolithic structure comprising porous walls that trap particulate matter as exhaust gas flows through. While DPFs are highly effective in capturing soot, their performance diminishes over time due to the progressive accumulation of particulate matter, which increases exhaust backpressure and adversely affects engine efficiency. To restore the filtering capacity, the trapped soot must be periodically removed through a regeneration process. However, passive thermal regeneration typically requires temperatures above 600 °C which are significantly higher than the normal operating

[a] *King Prajadhipok's Institute, Bangkok 10210, Thailand*
[b] *Faculty of Engineering and Technology, Pathumthani University, Pathumthani 12000, Thailand*
[c] *Chemical and Process Engineering, The Sirindhorn International Thai-German Graduate School of Engineering (TGGS), King Mongkut's University of Technology North Bangkok, Bangkok, 10800, Thailand. E-mail: unalome.w.cpe@tggs-bangkok.org*
[d] *Chemical Engineering, Engineering Faculty, King Mongkut's University of Technology North Bangkok, Bangkok, 10800, Thailand*

exhaust temperatures of 200–500 °C in diesel engines. This discrepancy necessitates the use of catalyzed diesel particulate filters (CDPFs), which lower the soot oxidation temperature, enabling regeneration at more practical operating conditions.[8]

In the context of catalysis for soot oxidation, various active materials have been extensively explored. Noble metals such as silver (Ag),[9] as well as rare earth oxides including cerium (Ce)[10] and lanthanum (La),[11] have demonstrated high catalytic efficiency. Nevertheless, their widespread application is constrained by critical limitations, including high cost, resource scarcity, and toxicity, which collectively impede commercial scalability. In response to these limitations, transition metal oxides such as cobalt oxide (Co_3O_4),[12] copper oxides (CuO_x),[13] iron oxide (Fe_2O_3),[14] and manganese oxides (MnO_x)[15] have emerged as promising alternatives. These materials offer notable advantages, including strong redox activity, excellent thermal stability, and superior performance in oxidation reactions.

Among the various transition metal oxides, manganese oxides (MnO_2, Mn_2O_3, Mn_3O_4 and MnO) have attracted considerable attention for soot oxidation applications due to their low cost, structural stability, and outstanding redox properties.[16,17] Catalytic activity in manganese oxides is strongly correlated with their oxidation states. Materials with a higher content of Mn^{4+} are generally more active, as Mn^{4+} ions facilitate enhanced oxygen mobility and rapid electron transfer. The increased surface concentration of Mn^{4+} is particularly beneficial in promoting the activation of oxygen species, which is essential for efficient oxidation reactions.[18]

The soot oxidation activity of manganese oxides could be enhanced by adjusting the dopant in the catalyst and varying its morphology or porosity structure. Nanostructured MnO_2 materials (*e.g.*, nanotubes, nanowires, nanoplates, nanorods) consistently exhibit superior catalytic activity over bulk particles due to their enhanced specific surface areas and higher density of exposed active sites, which improve reactant accessibility and facilitate catalytic reactions such as oxidation.[19,20] Liu *et al.*[21] reported that tube-like MnO_2 showed the highest specific surface area, enhanced redox properties, and increased surface-active oxygen species among various morphologies, resulting in improved catalytic oxidation. There are various synthesis techniques have been developed to produce metal oxide catalysts with tailored properties such as sol–gel,[22] co-precipitation,[23,24] and the hydrothermal method.[23] Among them, the hydrothermal method is widely favored for preparing nanostructured materials due to its ability to control morphology, achieve high crystallinity, high purity and narrow size distribution under mild conditions. It is also cost-effective and scalable.[25]

The catalytic activity of nanostructured MnO_2 materials can be further improved by incorporating other metals *via* doping, loading, or forming solid solutions. Doping manganese oxides with other metals can enhance catalytic properties by modifying the lattice structure, increasing oxygen vacancies, reducing particle agglomeration, and enhancing surface area.[26] Jampaiah *et al.*[27] showed that Cu and Co co-doping in α-MnO_2 nanowires significantly improved soot oxidation. Similarly, Zhang *et al.*[28] found that W and Cu doping increased Mn^{3+} content and oxygen vacancies, boosting catalytic activity. Among them, cobalt-doped MnO_2 has garnered significant attention for soot oxidation due to it has been reported to increase the concentration of surface-adsorbed oxygen species (O_2^-) and oxygen vacancies, which are vital for enhancing oxygen mobility. Furthermore, the strong electronic interaction between manganese and cobalt species contributes to improved reducibility, facilitating redox transitions such as Mn^{4+}/Mn^{3+} and Co^{3+}/Co^{2+} at lower temperatures, ultimately boosting catalytic efficiency for soot oxidation.[27] Cao *et al.*[29] reported the performance of transition-metal oxide nanosheets (Co, Mn, Fe) on the nickel foam for soot oxidation. They found that Co_3O_4 nanosheets on nickel foam outperformed other metals due to higher redox properties and abundant active oxygen species. Similarly, Neelapala *et al.*[26] demonstrated that Co-doped Mn_2O_3 catalysts enhanced specific surface area and multiple oxidation states of Mn and Co, leading to superior catalytic activity compared to pure Mn_2O_3.

In this work, MnO_2 nanowires were synthesized using the hydrothermal method and evaluated for their potential as catalysts in soot oxidation. To further enhance their catalytic performance, cobalt was introduced as a dopant to form Co/MnO_2 nanowire composites. The optimal dopant concentration was identified, and the influence of cobalt incorporation on the structural, morphological, and redox properties as well as the catalytic soot oxidation performance of the catalyst was thoroughly investigated.

2. Experimental section

2.1. MnO_2 nanowires synthesis

MnO_2 nanowire catalyst was synthesized using the hydrothermal method. In brief, 8 mmol of manganese sulfate ($MnSO_4 \cdot H_2O$), 20 mmol of ammonium sulfate ($(NH_4)_2SO_4$) and 8 mmol of ammonium persulfate ($(NH_4)_2S_2O_8$) were dissolved in 40 mL of DI water under magnetic stirring for 30 min until the precursor became a homogeneous solution. Then, the mixed solution was transferred to a Teflon-lined stainless-steel autoclave and heated at 140 °C for 8 h. After cooling to room temperature, the black precipitates were washed repeatedly with DI water and ethanol. Finally, the products were dried at 80 °C overnight.

2.2. Co-doped MnO_2 nanowires synthesis

Co-doped MnO_2 nanowire catalysts were also prepared using the hydrothermal method. Firstly, the as-prepared MnO_2 nanowires were dispersed in 35 mL of DI water and sonicated for 30 min. After that, cobalt nitrate hexahydrate [$Co(NO_3)_2 \cdot 6H_2O$], corresponding to 10 mol% Co and 20 mol% Co, was added into the above solution and kept under continuous stirring for 30 min. The pH of this solution was adjusted to 11 using ammonia solution. The resulting solution was transferred to a Teflon-lined stainless-steel autoclave and heated at 150 °C for 10 h. Finally, the prepared Co-doped MnO_2 nanowires sample

was dried at 80 °C overnight. The prepared 10 and 20 mol% Co-doped MnO_2 nanowires were labelled 10Co/Mn NWs and 20Co/Mn NWs, respectively.

2.3. Catalyst characterizations

The crystalline structures of the as-prepared catalysts were studied by X-ray diffraction (XRD) on a RIGAKU Smart Lab X-ray Diffractometer with Cu K_α radiation (λ = 1.542 Å). The operation voltage and current keep at 40 kV and 100 mA, respectively. The 2θ scan ranges of 20° to 80° with a scan speed of 5° min^{-1} and step width of 0.01° were used. The lattice strain (ε) of MnO_2 induced by the addition of Co can be calculated by Williamson–Hall (W–H) equation.[30] The morphologies of the as-prepared catalysts were carried out using filed emission scanning electron microscope (FE-SEM, JSM-7001F) with voltage of 20 kV and magnification of 100k×. N_2 adsorption–desorption isotherms were determined by V-Sorb 2800P Surface Area and Porosimetry Analyzer. Before the measurement, all catalysts were degassed under vacuum at 250 °C for 3 h. The specific surface areas were calculated using the Brunauer–Emmett–Teller (BET) method. The pore size distribution was estimated from the adsorption branch of the isotherms using the BJH model. The surface elemental compositions of samples were analyzed using X-ray photoelectron spectroscopy (XPS), PHI5000 VersaProbe II (ULVAC-PHI, Japan) at the SUT-NANOTEC-SLRI Joint Research Facility, Synchrotron Light Research Institute (SLRI), Thailand. Monochromatized Al-K_α X-ray source ($h\gamma$ = 1486.6 eV) was utilized to excite the samples. The survey spectra were recorded with an energy step of 1.000 eV and a pass energy of 117.4 eV, meanwhile, the high-resolution spectra were recorded with an energy step of 0.05 eV and a pass energy of 46.95 eV. The C 1s spectrum was used as the peak reference by marking the C–C/C–H at 284.8 eV. The reduction behaviors of the as-prepared catalysts were investigated using H_2-temperature programmed reduction (H_2-TPR). Before starting TPR process, 1.0 g of the catalyst in a quartz tube reactor was pretreated at 700 °C for 1 h with 100 mL min^{-1} of 10% O_2/Ar to eliminate surface impurities. After cooling to room temperature under Ar flow, 100 mL min^{-1} of 5% H_2/Ar was introduced, and the temperature was increased from 25 to 800 °C at a heating rate of 5 °C min^{-1}. H_2 consumption was analyzed using an on-line mass spectrometer (Omnistar, GSD 320 O1 Model). Oxygen vacancies and mobility in the catalyst were investigated using O_2-temperature programmed desorption (O_2-TPD) on the same instrument as H_2-TPR. Prior to each run, the sample was pretreated with 100 mL min^{-1} of 10% O_2/Ar at 700 °C for 1 h. After cooling to room temperature, the excess or physisorption of oxygen on the catalyst surface was eliminated by Ar flushing. The oxygen desorption amount was continuously monitored using an online mass spectrometer (Omnistar, GSD 320 O1 Model), while the temperature was ramped up from room temperature to 850 °C at a heating rate of 5 °C min^{-1}.

2.4. Catalytic activity evaluation

In this research, carbon black (Vulcan, XC 72R, average particle diameter of 50 nm) was used as the soot model for studying the soot combustion performance of the as-prepared catalyst with the tight contact mode. The soot and catalyst with weight ratio of 1 : 10 were mixed using a mortar and pestle for 10 min. The mixture was then loaded into a quartz tube and installed in the continuous flowed packed-bed reactor. The sample was heated to 700 °C (5 °C min^{-1}) under 100 mL min^{-1} of 10% O_2/Ar. The outlet gases (CO_2 and CO with m/z ratio of 44 and 28, respectively) were analyzed using a Mass spectrometer (Omnistar, GSD 320 O1 Model). The catalytic activity was evaluated by the temperatures at 10%, 50% and 90% conversion of soot which were denoted as T_{10}, T_{50} and T_{90}, respectively. The soot conversion can be calculated using the following equations:

$$\text{Soot conversion} = \frac{\int_{t=0}^{t=t_f}\left(\frac{dn_{CO_2}}{dt}\right) + \int_{t=0}^{t=t_f}\left(\frac{dn_{CO}}{dt}\right)}{\text{Initial carbon(mol)}} \times 100 \quad (1)$$

where, n_{CO_2} and n_{CO} represent the mole of CO and CO_2 species, respectively.

3. Results and discussion

3.1. Catalyst characterizations

3.1.1. Crystal structure analysis. Fig. 1 displays the XRD patterns of the as-prepared MnO_2 NWs, 10Co/Mn NWs, and 20Co/Mn NWs. The XRD patterns of MnO_2 NWs revealed mixed phases with dominant α-MnO_2 and minor γ-MnO_2. The diffraction angles (2θ) of 12.6°, 17.8°, 25.5°, 28.4°, 37.3°, 41.8°, 49.5°, 55.5°, 59.7°, 65.2° and 68.8° were indexed to the (110), (200), (220), (310), (211), (301), (411), (600), (521), (002) and (541) planes of α-MnO_2 (JCPDS no. 00-044-0141), respectively. The characteristic diffraction peaks of γ-MnO_2 were detected at 21.5°, 33.7° and 37.3°, which correspond to the (120), (031) and (131) planes (JCPDS no. 00-014-0644), respectively. The formation of mixed phases results in a higher concentration of surface defects compared to single-phase structures.[31] These

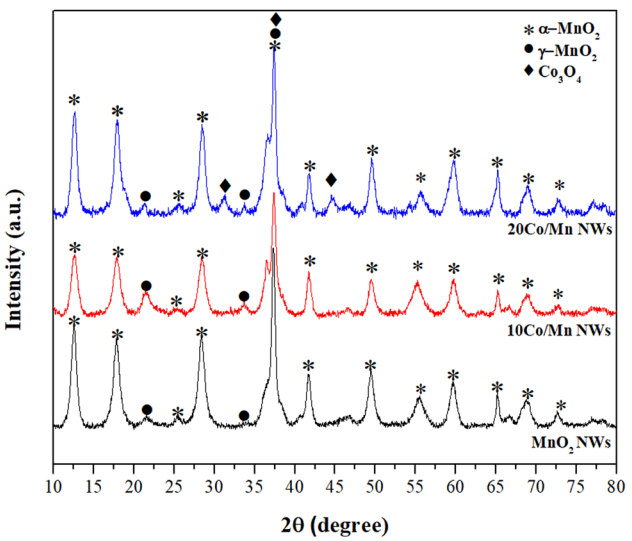

Fig. 1 XRD diffraction patterns of the as-prepared MnO_2 NWs, 10Co/Mn NWs and 20Co/Mn NWs catalysts.

defect sites typically serve as adsorption centers for surface oxygen species; therefore, an increased defect density facilitates the adsorption of oxygen molecules on the catalyst surface. For Co-doped MnO_2 NWs, characteristic diffraction peaks corresponding to mixed phases with predominantly α-MnO_2 and a minor γ-MnO_2 component were also observed. The 10Co/Mn NWs catalyst exhibited a more intense γ-MnO_2 peak than pure MnO_2 NWs, indicating a higher proportion of the γ-MnO_2 phase in the 10Co/Mn NWs sample. This enhanced γ-MnO_2 content is associated with an increased density of defect sites. The higher fraction of γ-MnO_2 observed in the 10Co/Mn NWs may result from the introduction of Co during the synthesis process using hydrothermal method, which could promote the partial transformation of α-MnO_2 into the γ-MnO_2 phase.[32] However, increasing Co loading to 20 mol% did not significantly influence the α-MnO_2 to γ-MnO_2 phase transformation, as indicated by the similar diffraction peak intensities of both phases in the 20Co/Mn and pure MnO_2 NWs catalysts. Notably, no diffraction peaks corresponding to Co_3O_4 were observed in the XRD pattern of the 10Co/Mn NWs catalyst, suggesting that the Co_3O_4 phase was either present at levels below the detection limit of the XRD instrument or highly dispersed on the MnO_2 NWs surface.[31] Moreover, the absence of Co_3O_4 peak probably indicated that Co substituted the Mn site in the MnO_2 lattice to form solid solution, which would lead to strain and unbalanced charge; therefore, oxygen vacancies or defects are expected to generate.

To investigate the lattice strain induced by cobalt doping in MnO_2 nanowires, Williamson–Hall (W–H) analysis was employed. Fig. S1 displays the W–H plots for pure MnO_2 and Co-doped MnO_2 nanowires, while the corresponding calculated strain values are summarized in Table 1. Notably, the Co-doped MnO_2 samples exhibit greater lattice strain compared to the undoped MnO_2, suggesting that the incorporation of Co ions into the MnO_2 lattice induces internal stress.[30] This phenomenon is likely attributed to the ionic radius mismatch between Mn and Co species. The resulting lattice distortion and strain not only confirm successful Co incorporation but also play a critical role in tuning the physicochemical properties of the catalyst. Specifically, such strain may facilitate the formation of oxygen vacancies and enhance lattice oxygen mobility, which is beneficial for catalytic soot oxidation. However, diffraction peaks characteristic of cubic Co_3O_4 were detected for 20Co/Mn NWs at 2θ values of 31.2°, 37.3°, and 44.6°, corresponding to the (200), (311), and (400) crystal planes, respectively (JCPDS no. 01-078-1969). The emergence of these Co_3O_4 peaks in the 20Co/Mn NWs catalyst implies a larger Co_3O_4 crystallite sizes and lower Co dispersion on the catalyst surface compared to the 10Co/Mn NWs, where larger particle sizes are typically less favorable for enhancing heterogeneous catalytic activity.[33]

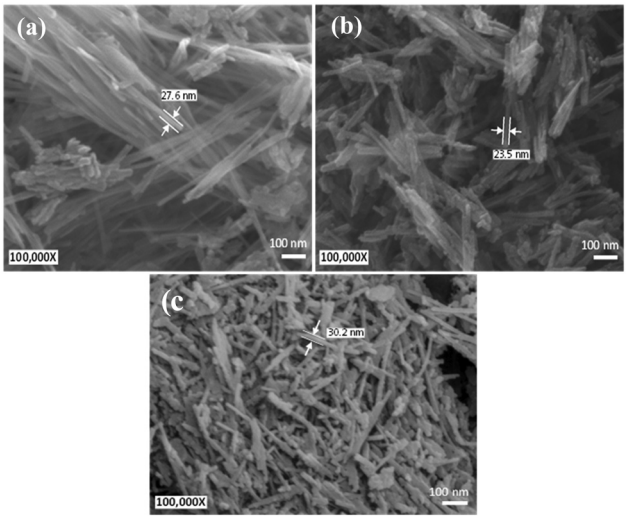

Fig. 2 SEM images of (a) pure MnO_2 NWs, (b) 10Co-Mn NWs and (c) 20Co/Mn NWs.

3.1.2. Morphology analysis. Scanning electron microscopy (SEM) was used to analyze the surface morphologies of the as-prepared MnO_2 NWs and Co-doped MnO_2 NWs catalysts, as shown in Fig. 2. As depicted in Fig. 2a, the pure MnO_2 NWs exhibited a densely packed network of randomly oriented nanowires. These nanowires possessed an average diameter of approximately 27.6 nm and extended several hundred nanometers in length, forming a uniform and interconnected structure. In contrast, Fig. 2b and c present the SEM micrographs of 10Co/Mn NWs and 20Co/Mn NWs, respectively. In these Co-doped samples, the nanowires displayed a tendency to form small aggregates or clusters, accompanied by partial fragmentation of the wire-like morphology.[34] This morphological change upon Co doping suggested a potential influence of cobalt on the structural integrity and dispersion of the MnO_2 nanowires.

3.1.3. N_2 adsorption–desorption analysis. Fig. 3 presents the N_2 adsorption–desorption isotherms of MnO_2 NWs, 10Co/Mn NWs, and 20Co/Mn NWs. According to the IUPAC classification,[35] all samples exhibited type IV isotherms with H3-type hysteresis loops, characteristic of mesoporous structures formed *via* capillary condensation. The textural parameters, including specific surface area, total pore volume, and average pore diameter, are summarized in Table 1. MnO_2 NWs showed a specific surface area of 33.8 $m^2\ g^{-1}$, a pore volume of 0.53 $cm^3\ g^{-1}$, and an average pore diameter of

Table 1 Lattice strain, specific BET surface area, pore volume and pore diameter of the catalysts

Catalyst	MnO_2 crystallite size (nm)	Lattice strain	Surface area ($m^2\ g^{-1}$)	Pore volume ($cm^3\ g^{-1}$)	Pore diameter (nm)
MnO_2 NWs	9.75	0.0008	33.8	0.53	44.8
10Co/Mn NWs	8.75	0.0027	36.0	0.57	46.3
20Co/Mn NWs	9.98	0.0021	61.1	0.59	38.9

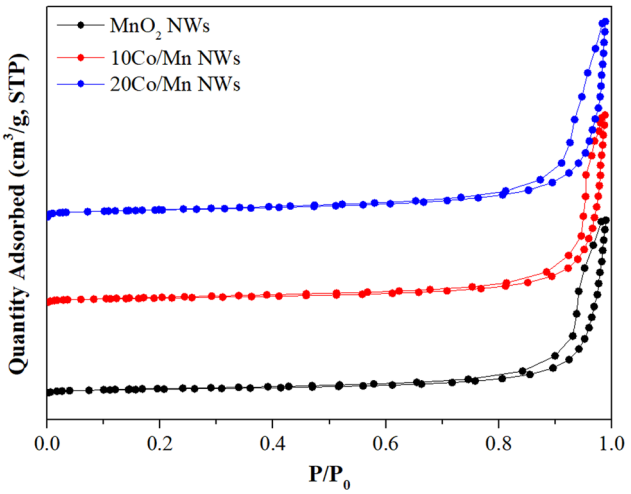

Fig. 3 N_2 adsorption–desorption isotherms of MnO_2 NWs, 10Co/Mn NWs and 20Co/Mn NWs catalysts.

44.8 nm. Doping with 10% Co led to an increase in these parameters, suggesting improved porosity and dispersion of Co species on the MnO_2 surface. These changes are attributed to the influence of Co incorporation on the formation of mesoporous structures, which are likely to enhance catalyst-soot contact and gas diffusion. Further increasing the Co loading to 20%, an increase of the surface area (61.1 $m^2\ g^{-1}$) and pore volume (0.59 $cm^3\ g^{-1}$), but a decrease in the average pore diameter to 38.9 nm was observed. While the larger surface area and pore volume generally favor catalytic activity, the smaller pore size may limit soot particle diffusion and reduce access to internal active sites.[36] Thus, achieving an optimal balance of surface area, pore volume, and pore diameter is critical for maximizing catalytic performance in soot combustion.

3.1.4. Surface elemental composition analysis. The surface elemental compositions of MnO_2 NWs, 10Co/Mn NWs, and 20Co/Mn NWs were examined using X-ray photoelectron spectroscopy (XPS). The Mn 2p XPS spectra for these samples are shown in Fig. 4(a)–(c). All catalysts exhibited two main spin–orbit doublet peaks at approximately 642 eV and 654 eV, corresponding to Mn $2p_{3/2}$ and Mn $2p_{1/2}$ transitions, respectively. Each of these peaks was further deconvoluted into three components, representing Mn^{2+}, Mn^{3+}, and Mn^{4+} oxidation states.[37–39] The combined ratio of Mn^{2+} and Mn^{3+} to total Mn species, which is indicative of oxygen vacancy formation, followed the order: 10Co/Mn (0.76) > 20Co/Mn (0.68) > MnO_2 (0.65) (Table 2). This trend implies a higher concentration of surface oxygen vacancies in the 10Co/Mn sample. The O 1s XPS spectra (Fig. 4(d)–(f)) of all catalysts were deconvoluted into three peaks centered around 530 eV, 531 eV, and 533 eV,

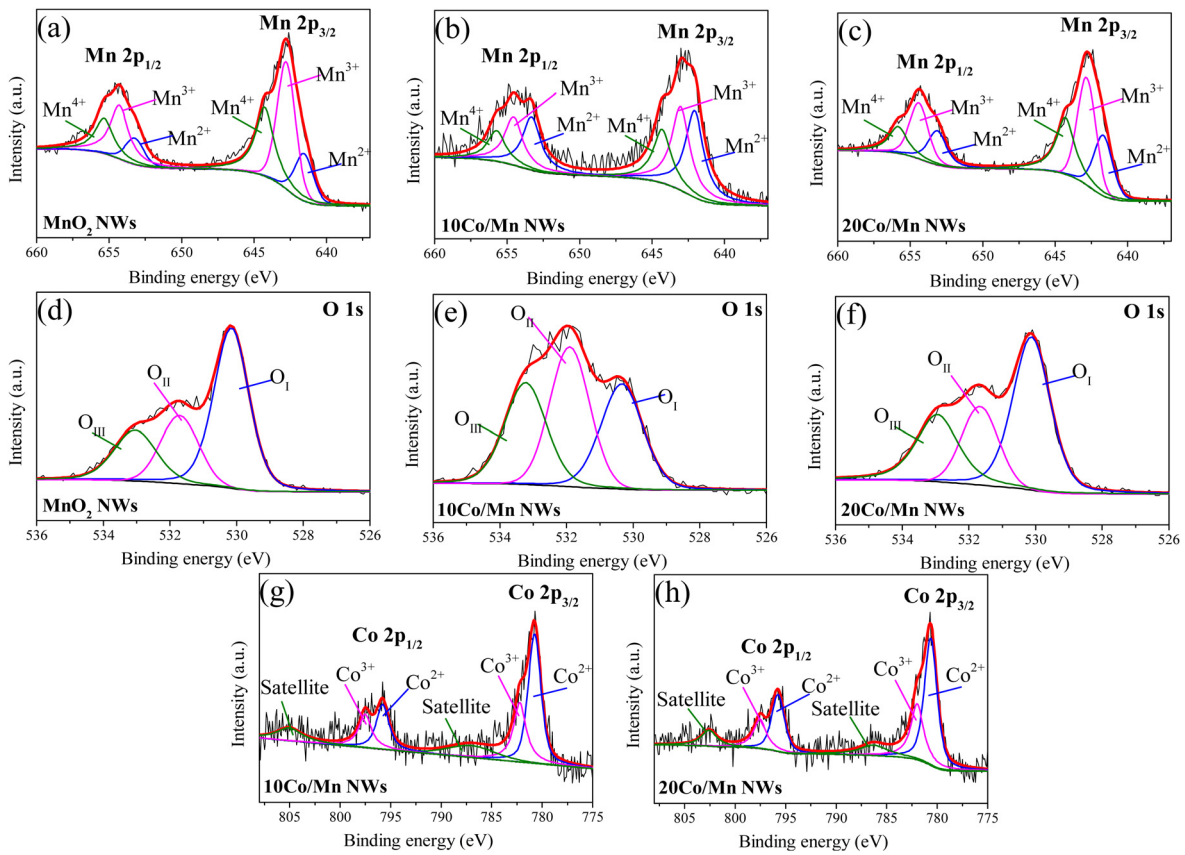

Fig. 4 XPS spectra of MnO_2 NWs, 10Co/Mn NWs and 20Co/Mn NWS: (a)–(c) high-resolution Mn 2p XPS spectra; (d)–(f) high-resolution O 1s XPS spectra; (g) and (h) high-resolution Co 2p.

Table 2 Surface element ratio calculated from XPS, H_2 consumption and desorbed O_2 of MnO_2 NWs, 10Co/MN NWs and 20Co/Mn NWs

Catalyst	$(Mn^{2+} + Mn^{3+})/(Mn^{4+} + Mn^{3+} + Mn^{2+})$	$O_{II}/(O_I + O_{II})$	$Co^{2+}/(Co^{2+} + Co^{3+})$	H_2 consumption (mmol g^{-1})	Desorbed O_2 (mmol g^{-1}) <600 °C
MnO_2 NWs	0.65	0.29	—	9.31	1.35
10Co/Mn NWs	0.76	0.54	0.65	7.22	2.55
20Co/Mn NWs	0.68	0.31	0.66	7.70	2.07

corresponding to lattice oxygen (O_I), surface adsorbed oxygen species associated with oxygen vacancies (O_{II}) which play an important role in soot catalytic combustion and are called reactive oxygen species, and surface carbonate/hydroxyl species (O_{III}), respectively.[40–42] The relative amount of surface adsorbed oxygen ($O_{II}/(O_I + O_{II})$) was highest for 10Co/Mn (0.54), followed by 20Co/Mn (0.31) and MnO_2 (0.29) (Table 2), correlating well with the Mn oxidation state analysis. Co 2p XPS spectra of Co-doped samples (Fig. 4(g) and (h)) revealed two spin–orbit doublets at approximately 780 eV (Co $2p_{3/2}$) and 796 eV (Co $2p_{1/2}$), along with two satellite peaks near 786 eV and 802 eV. Deconvolution of the Co 2p peaks identified the presence of both Co^{2+} and Co^{3+} oxidation states.[43,44] The ratio of Co^{2+} to total Co species is presented in Table 2. The XPS results confirm that cobalt incorporation into MnO_2 nanowires significantly enhances surface oxygen vacancy concentrations, especially at 10 mol% loading, by modifying the Mn oxidation states and increasing the proportion of surface reactive oxygen species. However, excessive Co doping (20 mol%) reduces the generation of oxygen vacancies, likely due to structural saturation or phase segregation. Therefore, moderate cobalt doping (10 mol%) is optimal for promoting defect formation and enhancing catalytic performance in soot oxidation.

3.1.5. H_2-TPR analysis. The redox property of a catalyst is an important factor in evaluating catalytic activity for soot oxidation, as it governs the mobility and availability of active oxygen species. This characteristic is commonly assessed using hydrogen-temperature programmed reduction (H_2-TPR). Fig. 5 presents the H_2-TPR profiles of the synthesized catalysts,

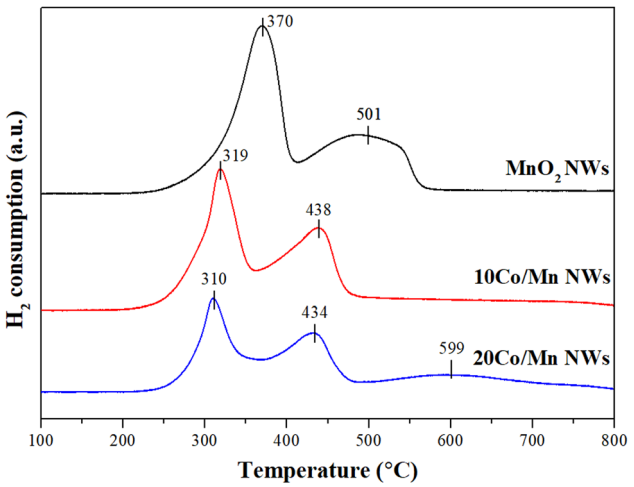

Fig. 5 H_2-TPR Profiles of the pure MnO_2, 10Co/Mn, and 20Co/Mn NWs catalysts.

revealing the reduction of surface and bulk lattice oxygen species with increasing temperature under a hydrogen atmosphere. For the undoped MnO_2 nanowires, two reduction peaks were observed. The first reduction peaks at lower temperatures of 370 °C is attributed to the reduction of the surface and bulk oxygen species of MnO_2 to Mn_3O_4. The second, broader reduction peak at high temperature of 501 °C, is ascribed to the subsequent reduction of Mn_3O_4 to MnO, in agreement with previously reported studies on similar nanowire morphologies.[27,45]

Upon cobalt incorporation, the reduction peak of the catalyst also showed a two-stage reduction peak at 319 and 438 °C for 10Co/Mn NWs and at 310 and 434 °C for 20Co/Mn NWs. These shifts toward lower reduction temperatures compared to pure MnO_2 NWs suggested enhanced reducibility, likely arising from the synergistic effects between Mn and Co species probably through the formation of solid solutions, as supported by X-ray diffraction (XRD) analysis. The presence of such a solid solution is known to promote the generation of oxygen vacancies and to enhance the mobility of lattice oxygen, thereby facilitating its migration from the bulk to the catalyst surface.[27] This improved oxygen transport capability enables a more dynamic redox cycle, accelerating the redox reaction process. The resultant increase in oxygen vacancies contributes significantly to the overall catalytic activity for soot oxidation, as the vacancies provide active sites for oxygen adsorption and facilitate rapid oxygen exchange.[46]

Interestingly, the 20 mol% Co-doped catalyst exhibited the lowest reduction temperature among the three samples, reflecting even greater reducibility. However, despite its superior redox properties, the 20Co/Mn NWs catalyst showed lower soot oxidation activity compared to 10Co/Mn NWs. This discrepancy can be attributed to structural and textural properties. At higher Co loadings, excessive cobalt species may aggregate into larger crystallites sizes, reducing the number of accessible active sites and impairing the intimate contact between the catalyst and soot. Furthermore, the decreased average pore diameter in 20Co/Mn NWs may limit soot accessibility and diffusion, diminishing the catalytic efficiency despite enhanced redox behavior.[36]

In addition, the reduction peak observed around 300 °C in the Co-doped catalysts is likely associated with the reduction of Co^{3+} to Co^{2+}, which overlaps with the reduction features of MnO_2.[47] Furthermore, the broad peak at around 599 °C for 20Co/MN NWs can be attributed to the further reduction of Co^{2+} in bulk to metallic Co^0, consistent with literature reports.[48] However, the temperature of completely soot combustion is lower than 450 °C (Fig. 7a), so the reduction of Cobalt

in the bulk has no effect on the soot catalytic combustion. The calculated hydrogen consumption of pure MnO_2 NWs, 10Co/Mn NWs and 20Co/Mn NWs were 9.31, 7.22 and 7.70 mmol g_{cat}^{-1}, respectively (Table 2). The lower H_2 consumption observed for the Co-doped catalysts relative to the undoped MnO_2 NWs suggested the higher Mn^{3+} amount in the catalyst structure, corresponding to XPS results. It is well established that the existence of Mn^{3+} in MnO_2 resulted in the generation of oxygen vacancies to maintain charge neutrality,[31] which further supports the enhanced redox behavior and improved catalytic performance observed in the Co-doped systems.

3.1.6. O_2-TPD analysis. To investigate the nature and mobility of surface and lattice oxygen species, O_2-temperature programmed desorption (O_2-TPD) experiments were carried out for the synthesized catalysts. Understanding the oxygen desorption behavior is crucial, as the catalytic combustion of soot primarily involves oxidation reactions that depend heavily on the availability and reactivity of oxygen species. As shown in Fig. 6, the desorption peak observed in the temperature range of 400–600 °C is attributed to labile oxygen species associated with surface or subsurface oxygen vacancies, which are considered highly reactive and play a key role in low-temperature oxidation. In contrast, the peak detected above 700 °C corresponds to the release of lattice oxygen, which is more strongly bound within the crystal structure and generally exhibits lower reactivity.

Quantitative analysis of the O_2-TPD profiles was performed by integrating the peak areas within the 400–600 °C range to estimate the amount of surface-active oxygen species, with the results summarized in Table 2. The trend in desorbed O_2 content follows the order: 10Co/Mn NWs > 20Co/Mn NWs > MnO_2 NWs. This indicates that the incorporation of 10% Co into MnO_2 significantly enhances the generation of oxygen vacancies, thereby increasing the availability of reactive surface oxygen. This observation is in agreement with the XPS analysis, which also confirmed a higher proportion of surface oxygen species in the 10Co/Mn NWs catalyst, which contributed directly to its improved soot oxidation performance.

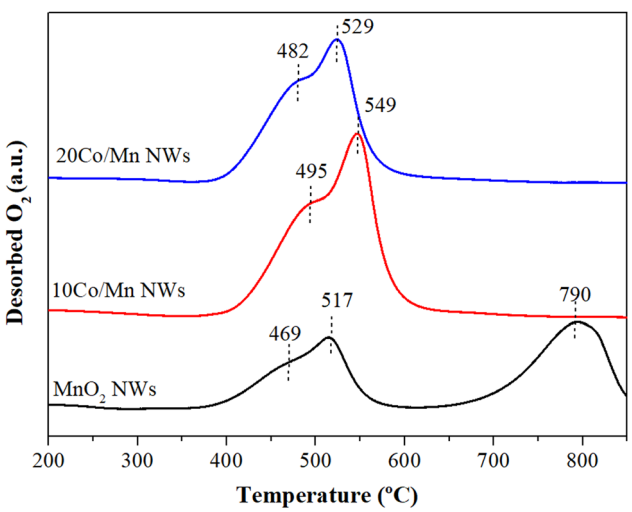

Fig. 6 O_2-TPD profiles of the pure MnO_2, 10Co/Mn, and 20Co/Mn NWs catalysts.

3.2. Catalytic activity

The catalytic performance of MnO_2 and Co-doped MnO_2 nanowire catalysts for soot oxidation was evaluated by analyzing the soot conversion profiles and determining the temperatures at 10%, 50%, and 90% soot conversion (denoted as T_{10}, T_{50}, and T_{90}, respectively) under tight contact conditions. These temperatures are commonly defined as the ignition temperature (T_{10}), the combustion temperature (T_{50}), and the maximum conversion temperature (T_{90}), and are critical indicators for assessing the catalytic efficiency in soot oxidation reactions. For comparison, non-catalyzed soot oxidation was also examined under identical conditions.

Fig. 7(a) and Fig. S2 present the soot conversion curves for all samples, revealing that the Co-doped and undoped MnO_2 nanowires catalysts significantly enhance the oxidation of soot at lower temperatures compared to the non-catalyzed reaction.

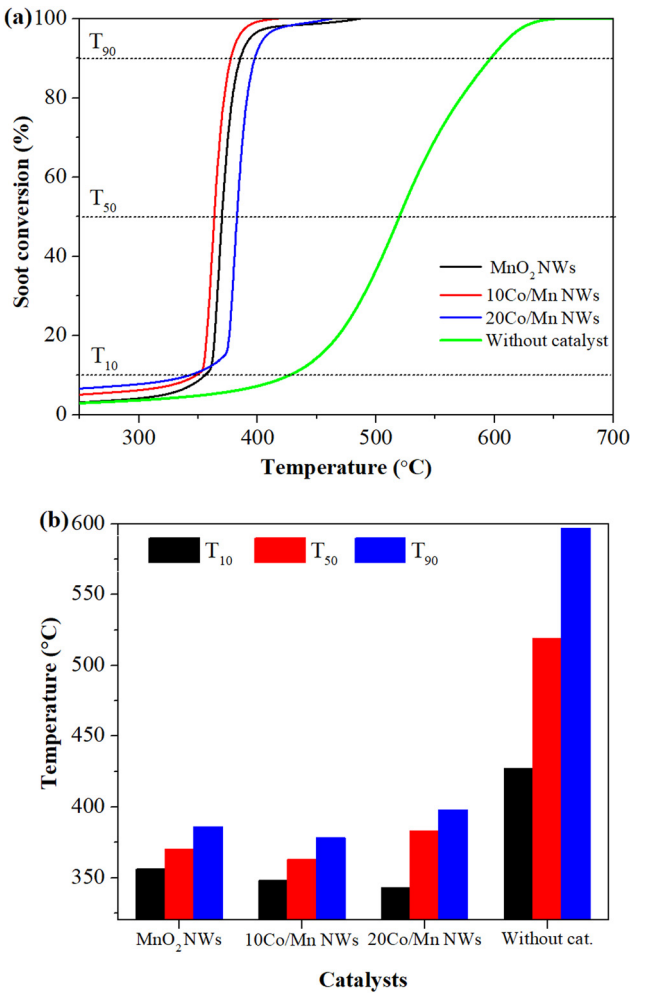

Fig. 7 Soot oxidation activities of the catalyst under tight contact conditions (soot: catalyst ratio of 1 : 10) in terms of (a) soot conversion and (b) T_{10}, T_{50} and T_{90} values.

This enhanced activity can be primarily attributed to the nanowire morphology of MnO_2, which offers a high specific surface area, facilitating more effective contact between the catalyst and soot particles. This improved contact promotes the generation and mobility of reactive oxygen species that facilitate the conversion of soot.

The T_{10}, T_{50}, and T_{90} values for all catalysts are summarized in Fig. 7(b) and Table S1. Among the tested samples, the T_{50} values followed the order: 10Co/Mn NWs (363 °C) < 5Co/MN NWs (365 °C) < Co_3O_4 (366 °C) < MnO_2 NWs (370 °C) < 20Co/Mn NWs (383 °C) < uncatalyzed soot (519 °C). The 10 mol% Co-doped MnO_2 nanowires exhibited superior low-temperature soot combustion performance compared to pure MnO_2 and Co_3O_4, indicating that cobalt incorporation significantly promotes catalytic activity. This enhancement is attributed to the synergistic effects between manganese and cobalt species, which collectively improve oxygen mobility, structural defects (*e.g.*, oxygen vacancies), and the redox properties of the catalyst. These features facilitate more efficient oxygen activation and transfer during soot oxidation. However, the lower performance at 5 mol% Co can be attributed to insufficient redox enhancement, limited oxygen vacancy creation, and lower density of active sites compared to the 10 mol% system.

Conversely, the 20 mol% Co-doped MnO_2 nanowires showed reduced catalytic activity, with soot oxidation occurring at higher temperatures than pure MnO_2 NWs and 10Co/Mn NWs. This decline in activity is likely due to the excessive cobalt loading, which leads to poor dispersion, smaller pore size and weak interaction between Co and the MnO_2 support, as evidenced by XRD and N_2 adsorption–desorption results. Moreover, excessive Co doping also reduces the generation of oxygen vacancies, as discussed in the XPS and O_2-TPD results. These factors outweigh the potential benefits of cobalt doping, highlighting the importance of optimizing the dopant concentration to maintain the structural and redox balance necessary for effective soot oxidation. Therefore, moderate cobalt doping (10 mol%) is optimal for promoting defect formation and enhancing catalytic performance in soot oxidation. Table 3 provides a comparative overview of soot oxidation performances reported in the literature for various Mn-based catalysts. The T_{10}, T_{50}, and T_{90} values vary depending on the catalyst morphology and the nature of metal doping, which together influence the surface area and the availability of reactive oxygen species, ultimately determining the catalytic efficiency.

3.3. Catalytic soot combustion mechanism

The mechanism underlying catalytic soot oxidation over the prepared catalysts is proposed to follow the Mars–van Krevelen (MvK) pathway, a well-established model for oxidation reactions on metal oxide catalysts.[49] In this mechanism, the availability and reactivity of lattice oxygen species are crucial determinants of the overall catalytic performance, particularly in oxidation reactions involving solid carbonaceous materials like soot. The catalytic oxidation of soot involves a sequence of elementary steps that occur both in the gas phase and on the surface of the catalyst. Initially, soot particles are adsorbed onto the catalyst surface, forming a surface-bound carbon species. This is followed by a redox interaction between the adsorbed soot and surface-active oxygen species (denoted as O_{sur}), resulting in the formation of gaseous carbon oxides (CO or CO_2) and the concurrent generation of oxygen vacancies (O_v) on the catalyst surface, as shown in the following simplified reactions:

$$C_{soot} + O_{sur} \rightarrow CO + O_v \quad (2)$$

$$C_{soot} + 2O_{sur} \rightarrow CO_2 + 2O_v \quad (3)$$

Following the consumption of surface oxygen species in soot oxidation, the lattice oxygen from the bulk of the catalyst migrates to the surface to replenish the oxygen vacancies. This oxygen migration restores catalytic activity by regenerating surface-active oxygen species, thereby sustaining the oxidation cycle. Additionally, the presence of oxygen vacancies provides favorable adsorption sites for O_2 molecules from the gas phase. Once adsorbed, O_2 molecules are activated and dissociated into reactive oxygen species, which further contribute to soot oxidation by reacting with carbonaceous species at the catalyst-soot interface.

Therefore, the superior catalytic activity of the 10Co/Mn NWs catalyst can be attributed to several synergistic factors: (i) the 10Co/Mn NWs exhibited a highly dispersed of cobalt on the MnO_2 nanowire support with a smaller nanowire diameter and larger pore size which facilitates improved contact between the soot particles and catalyst surface, enhancing mass transfer and the accessibility of active sites. (ii) The incorporation of Co into the MnO_2 nanowire structure promoted the generation of oxygen vacancies and enhanced the reducibility of the catalyst. These vacancies not only serve as active sites for O_2 adsorption and activation but also support a more efficient migration of lattice oxygen, which is essential for sustaining the MvK redox

Table 3 Comparison of soot oxidation activities of Mn-based catalysts in literature and this work

Catalysts	Morphologies	Reactant	T_{10} (°C)	T_{50} (°C)	T_{90} (°C)	Ref.
10Co/Mn	Nanowires	10% O_2/Ar	348	363	378	This work
1% Co/MnO_x	Nanorods	10% O_2/N_2	345	396	447	52
Co–Mn-600	Nanocomposites	21% O_2/N_2	368	469	513	53
MnO_2	Nanowires	10% O_2/Air	480	528	575	27
5Co–MnO_2			425	513	550	
10Co–MnO_2			420	475	530	
20Co–MnO_2			475	547	560	
MnO_x–CeO_2	Nanorods	O_2/Air	391	442	542	54
Ag/α-MnO_2	Nanoflower	10% O_2/Ar	439	509	608	55

cycle during soot oxidation. Collectively, these attributes result in improved catalytic performance for the 10Co/Mn NWs, enabling more efficient oxidation of soot at lower temperatures.

3.4. Stability of the catalyst after soot combustion test

To evaluate the structural and morphological stability of MnO_2 nanowires under soot combustion conditions, both scanning electron microscopy (SEM) and X-ray diffraction (XRD) were conducted, as illustrated in Fig. 8. These characterizations aimed to confirm the retention of the catalyst's crystalline structure and morphology before and after catalytic testing. Fig. 8(a) shows the SEM image of a physical mixture of MnO_2 NWs and carbon black, prepared at a catalyst:soot mass ratio of 1 : 10 under tight contact conditions, prior to the soot combustion reaction. The image clearly displays the nanowire structure of MnO_2 entangled with spherical carbon black particles. This intimate contact between soot and catalyst is favorable for catalytic oxidation due to enhanced surface interactions. Following the soot oxidation reaction at temperature of 410 °C (complete combustion), the morphology of the spent catalyst was re-examined by SEM, as shown in Fig. 8(b). Remarkably, the nanowire morphology of MnO_2 was preserved, with the diameters remaining close to their original dimensions. This observation confirms the outstanding thermal and morphological stability of MnO_2 NWs under reaction conditions.

To further assess the crystallographic stability, XRD patterns of both the fresh and spent catalysts were obtained, as presented in Fig. 8(c). The XRD pattern of the fresh MnO_2 NWs exhibited diffraction peaks corresponding to the MnO_2 phase, as previously discussed in the catalyst characterization section. However, after soot combustion at 410 °C (complete combustion), the diffraction pattern of the used catalyst showed new peaks at 2θ values of 18.0°, 28.9°, 31.0°, 32.3°, 36.1°, 38.0°, 44.4°, 50.7°, 58.5°, 59.8°, and 64.6°, which can be indexed to the (101), (112), (200), (103), (211), (004), (220), (105), (321), (224), and (400) planes of the Mn_3O_4 crystalline phase (JCPDS no. 00-071-0588). This phase transformation from MnO_2 to Mn_3O_4 is consistent with the high-temperature reductive environment encountered during soot combustion.

To elucidate the catalytic role of Mn_3O_4 in soot oxidation, a combustion activity test using pure Mn_3O_4 was carried out. As shown in Fig. S2 and Table S1, pure Mn_3O_4 exhibits measurable catalytic activity, indicating that the catalyst remains active even after the phase transition from MnO_2 to Mn_3O_4 during the reaction. Mn_3O_4 is a mixed-valence oxide containing both Mn^{2+} and Mn^{3+} species, and its spinel structure is characterized by a higher concentration of oxygen vacancies and enhanced oxygen mobility compared to MnO_2, particularly under high-temperature or reducing conditions. Although Mn_3O_4 possesses a lower intrinsic oxidation potential than MnO_2, its ability to generate and transport active oxygen species which facilitated by the Mn^{3+}/Mn^{2+} redox couple plays a crucial role in sustaining catalytic activity. Similar to MnO_2, soot oxidation over Mn_3O_4 proceeds *via* the Mars–van Krevelen (MvK) mechanism,[50] as previously discussed. Wagloehner and co-workers[51] have also demonstrated that Mn_3O_4 possesses

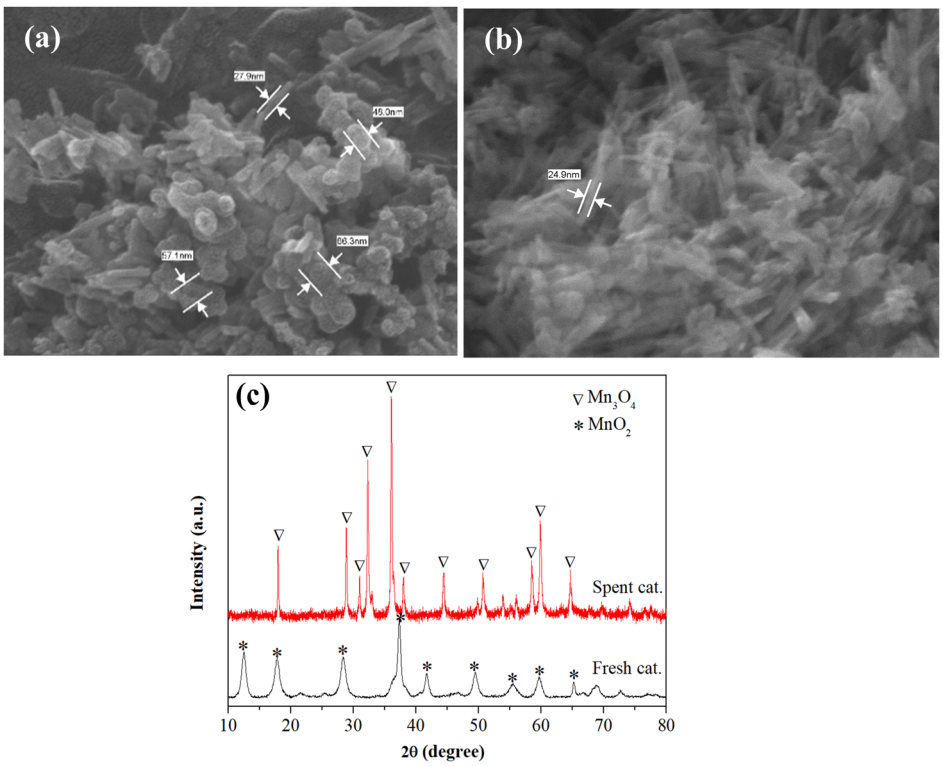

Fig. 8 SEM images of carbon black (Vulcan, XC 72R) mixed with MnO_2 NWs catalyst before (a) and after (b) soot combustion and (c) XRD of Fresh MnO_2 NWs compare to spent catalyst.

comparable catalytic performance to MnO_2 in soot combustion reactions due to its favorable redox properties and the ability to generate and transport active oxygen species. Therefore, the formation of the Mn_3O_4 phase does not compromise the long-term functionality of the catalyst and may enable stable catalytic performance over multiple reaction cycles.

4. Conclusions

In this study, Co-doped MnO_2 nanowires were synthesized *via* a hydrothermal method and systematically evaluated for their structural, redox, and catalytic properties in soot oxidation. XRD analysis revealed that Co incorporation promoted the formation of mixed α-MnO_2 and γ-MnO_2 phases and solid solution structure, which induced the generation of structural defects. SEM images confirmed that the nanowire morphology was retained after Co doping, though partial fragmentation and aggregation were observed with increasing Co content. Catalytic activity tests demonstrated that 10Co/Mn NWs exhibited the best soot oxidation performance, achieving the lowest T_{50} (363 °C). This enhancement is attributed to the optimized balance of textural properties, increased surface oxygen vacancy concentration, and superior oxygen mobility, as supported by N_2 adsorption–desorption, H_2-TPR, O_2-TPD, and XPS analysis. Although further Co doping (20 mol%) improved reducibility, the decline in soot oxidation performance was linked to excessive cobalt loading, which likely induced structural saturation, decreased average pore size, and limited soot-catalyst contact due to Co agglomeration. Notably, the catalyst preserved its nanowire morphology and remained catalytically active after reaction, transitioning to Mn_3O_4. Overall, these findings demonstrate that moderate Co doping (10 mol%) optimally tunes the physicochemical properties of MnO_2 nanowires, enhancing their catalytic efficiency for soot oxidation. This work also highlights the catalytic relevance of Mn_3O_4 as a durable post-reaction phase, supporting the long-term applicability of Mn-based nanostructures in environmental catalysis.

Author contributions

Issara Sereewatthanawut: writing – original draft, resources, project administration. Chalempol Khajonvittayakul: validation, methodology, investigation, formal analysis. Notsawan Swadchaipong: validation, project administration. Vut Tongnan: writing – original draft, validation, methodology, investigation, formal analysis, data curation. Panupun Maneesard: writing – original draft, validation, methodology, investigation, formal analysis, data curation. Rossarin Ampairojanawong: writing – review & editing, validation, formal analysis, data curation. Tawiwan Kangsadan: writing – review & editing, supervision. Matthew Hartley: writing – review & editing, supervision. Ammarika Makdee: writing – review & editing, visualization, investigation, formal analysis, data curation, conceptualization. Unalome Wetwatana Hartley: writing – review & editing, supervision, resources, project administration, funding acquisition, conceptualization.

Conflicts of interest

There are no conflicts to declare.

Data availability

The data supporting this article have been included as part of the SI.

Williamson-Hall plots of all catalysts, soot conversion and values of T_{10}, T_{50} and T_{90} for Co_3O_4, Mn_3O_4 and 5Co/Mn NWs compared to the best catalyst (10Co/Mn NWs). See DOI: **https://doi.org/10.1039/d5ma00480b**

Acknowledgements

This research has received funding support from King Mongkut's University of Technology North Bangkok; KMUTNB (contract number KMUTNB-FF-66-52), National Research Council of Thailand; NRCT (contact number N83A670023 and N84A680761); Program Management Unit for Competitiveness; PMUC (contact number C23F670095) and the International Science Partnerships Fund (ISPF *via* the British Council). Special thanks to the scientists at the SUT-NANOTEC-SLRI Joint Research Facility, Synchrotron Light Research Institute (SLRI), Thailand for their technical assistance and beam-time support

References

1 E. Vouitsis, L. Ntziachristos and Z. Samaras, *Prog. Energy Combust. Sci.*, 2003, **29**, 635–672.
2 B. A. A. L. Van Setten, M. Makkee and J. A. Moulijn, *Catal. Rev.*, 2001, **43**, 489–564.
3 B. Guan, R. Zhan, H. Lin and Z. Huang, *J. Environ. Manage.*, 2015, **154**, 225–258.
4 A. I. Totlandsdal, M. Lag, E. Lilleaas, F. Cassee and P. Schwarze, *Environ. Toxicol.*, 2015, **30**, 188–196.
5 A. J. Lucking, M. Lundback, N. L. Mills, D. Faratian, S. L. Barath, J. Pourazar, F. R. Cassee, K. Donaldson, N. A. Boon, J. J. Badimon, T. Sandstrom, A. Blomberg and D. E. Newby, *Eur. Heart J.*, 2008, **29**, 3043–3051.
6 J. Kagawa, *Toxicology*, 2002, **181–182**, 349–353.
7 D. Fino, S. Bensaid, M. Piumetti and N. Russo, *Appl. Catal., A*, 2016, **509**, 75–96.
8 Neha, R. Prasad and S. V. Singh, *J. Environ. Chem. Eng.*, 2020, **8**, 103945.
9 S. K. Megarajan, S. Rayalu, M. Nishibori, Y. Teraoka and N. Labhsetwar, *ACS Catal.*, 2015, **5**, 301–309.
10 A. Bueno-López, *Appl. Catal., B*, 2014, **146**, 1–11.
11 Q. Wu, J. Xiong, Y. Zhang, X. Mei, Y. Wei, Z. Zhao, J. Liu and J. Li, *ACS Catal.*, 2019, **9**, 3700–3715.
12 J. C. Medina, S. E. Rodil and R. Zanella, *Catal. Sci. Technol.*, 2020, **10**, 853–863.

13 Y. Yu, M. Meng and F. Dai, *Nanoscale*, 2013, **5**, 904–909.
14 P. Stelmachowski, A. Kopacz, P. Legutko, P. Indyka, M. Wojtasik, L. Ziemiański, G. Zak, Z. Sojka and A. Kotarba, *Catal. Today*, 2015, **257**, 111–116.
15 W. Si, Y. Wang, Y. Peng, X. Li, K. Li and J. Li, *Chem. Commun.*, 2015, **51**, 14977–14980.
16 H. Deng, S. Kang, J. Ma, C. Zhang and H. He, *Appl. Catal., B*, 2018, **239**, 214–222.
17 F. D. Speck, P. G. Santori, F. Jaouen and S. Cherevko, *J. Phys. Chem. C*, 2019, **123**, 25267–25277.
18 R. T. Guo, Q. L. Chen, H. L. Ding, Q. S. Wang, W. G. Pan, N. Z. Yang and C. Z. Lu, *Catal. Commun.*, 2015, **69**, 165–169.
19 T. Zhao, Y. Li, C. Wu, W. Cao, J. Gong, M. Xiao, Z. Song, Z. Shao, M. Zhao and B. Cui, *Green Energy Environ.*, 2025, **10**, 1481–1502.
20 K. Li, C. Chen, H. Zhang, X. Hu, T. Sun and J. Jia, *Appl. Surf. Sci.*, 2019, **496**, 143662.
21 S. Liu, M. Li, Y. Xiong and Y. Zhu, *ACS Appl. Nano Mater.*, 2023, **6**, 14721–14732.
22 Y. Gao, X. Wu, S. Liu, D. Weng, H. Zhang and R. Ran, *Catal. Today*, 2015, **253**, 83–88.
23 J. Wang, C. Zhang, Y. Wang, W. Chen, Z. Li and Y. Feng, *Catal. Lett.*, 2021, **151**, 3261–3272.
24 S. Ali, X. Wu, Z. Zuhra, Y. Ma, Y. Abbas, B. Jin, R. Ran and D. Weng, *Appl. Surf. Sci.*, 2020, **512**, 145602.
25 M. Yoshimura and K. Byrappa, *J. Mater. Sci.*, 2008, **43**, 2085–2103.
26 S. D. Neelapala, H. Patnaik and H. Dasari, *Asia-Pac. J. Chem. Eng.*, 2018, **13**, 1–9.
27 D. Jampaiah, V. K. Velisoju, P. Venkataswamy, V. E. Coyle, A. Nafady, B. M. Reddy and S. K. Bhargava, *ACS Appl. Mater. Interfaces*, 2017, **9**, 32652–32666.
28 C. Li, R. Li, Y. Wang, R. Niu, Q. Guo and C. Zhang, *J. Ind. Eng. Chem.*, 2023, **126**, 454–464.
29 C. Cao, L. Xing, Y. Yang, Y. Tian, T. Ding, J. Zhang, T. Hu, L. Zheng and X. Li, *Appl. Surf. Sci.*, 2017, **406**, 245–253.
30 A. Makdee, P. Unwiset and K. Chayakul, *Mater. Chem. Phys.*, 2018, **213**, 431–443.
31 X. Li, J. Ma, L. Yang, G. He, C. Zhang, R. Zhang and H. He, *Environ. Sci. Technol.*, 2018, **52**, 12685–12696.
32 S. M. Jadhav, R. S. Kalubarme, N. Suzuki, C. Terashima, J. Mun, B. B. Kale, S. W. Gosavi and A. Fujishima, *ACS Omega*, 2021, **6**, 5717–5729.
33 X. Zhu, X. Wu, J. Liu, J. Luo, Z. Yang, Y. Jiang and G. Chen, *Catalysts*, 2022, **12**, 1–14.
34 M. H. Ahmad, M. R. Islam and M. R. Islam, *Arab. J. Sci. Eng.*, 2024, **50**, 583–596.
35 M. Thommes, K. Kaneko, A. V. Neimark, J. P. Olivier, F. Rodriguez-Reinoso, J. Rouquerol and K. S. W. Sing, *Pure Appl. Chem.*, 2015, **87**, 1051–1069.
36 S. Zhou, L. Wang, S. Gao, X. Chen, C. Zhang, D. Yu, X. Fan, X. Yu and Z. Zhao, *ACS Catal.*, 2024, **14**, 6062–6127.
37 H. Su, J. Liu, Y. Hu, T. Ai, C. Gong, J. Lu and Y. Luo, *Nanomaterials*, 2023, **13**, 775.
38 J. Wang, C. Zhang, S. Yang, H. Liang and Y. Men, *Catal. Sci. Technol.*, 2019, **9**, 6379–6390.
39 Y. Zhu, Z. Chen, H. Li, Q. Wang, X. Liu, Y. Hu, C. Su, R. Duan, S. Chen and L. Lan, *Sci. Rep.*, 2023, **13**, 1–13.
40 P. Kaisook, P. Athikaphan, S. Nijpanich, T. Minato, S. Neramittagapong and A. Neramittagapong, *Results Eng.*, 2025, **25**, 103795.
41 M. Wang, J. Wang, Y. Zhang, Y. Yu and W. Shan, *Catal. Sci. Technol.*, 2024, **14**, 6278–6285.
42 A. Yusuf, Y. Sun, Y. Ren, C. Snape, C. Wang, H. Jia and J. He, *J. Phys. Chem. C*, 2020, **124**, 26320–26331.
43 H. S. Jadhav, S. M. Pawar, A. H. Jadhav, G. M. Thorat and J. G. Seo, *Sci. Rep.*, 2016, **6**, 2–13.
44 J. Luo, X. Zhu, Z. Zhong, G. Chen, Y. Hong and Z. Zhou, *Molecules*, 2024, **29**, 1–14.
45 Y. Cui, H. Song, Y. Shi, P. Ge, M. Chen and L. Xu, *Nanomaterials*, 2022, **12**, 2083.
46 H. Chi, P. Zhang, J. Xiong, Y. Wei, Y. Li, Z. Zhao, J. Liu and J. Jiao, *Appl. Surf. Sci.*, 2023, **608**, 155116.
47 K. Xu, M. Wang, Y. Zhang, W. Shan and H. He, *Ind. Eng. Chem. Res.*, 2021, **60**, 11412–11420.
48 X. Zhu, X. Gao, X. Yu, C. Zheng and X. Tu, *Catal. Today*, 2015, **256**, 108–114.
49 X. Zhang, M. Zhao, Z. Song, H. Zhao, W. Liu, J. Zhao, Z. Ma and Y. Xing, *New J. Chem.*, 2019, **43**, 10868–10877.
50 M. Rotko and K. Karpińska-Wlizło, *Molecules*, 2025, **30**, 343.
51 S. Wagloehner, M. Nitzer-Noski and S. Kureti, *Chem. Eng. J.*, 2015, **259**, 492–504.
52 M. Wang, Y. Zhang, Y. Yu, W. Shan and H. He, *Environ. Sci. Technol.*, 2021, **55**, 240–248.
53 L. Wang, Y. Wu, N. Feng, J. Meng, H. Wan and G. Guan, *RSC Adv.*, 2016, **6**, 50288–50296.
54 W. Shan, N. Ma, J. Yang, X. Dong, C. Liu and L. Wei, *J. Nat. Gas Chem.*, 2010, **19**, 86–90.
55 Y. Wang, Y. Wang, L. Zhang, C. Zhang, C. Zhang, X. Xu, Y. Xie, Y. Xie, W. Chen, W. Chen, J. Wang, J. Wang, R. Zhang and R. Zhang, *Ind. Eng. Chem. Res.*, 2020, **59**, 10407–10417.